Conti *et al. Heritage Science* (2022) 10:128
https://doi.org/10.1186/s40494-022-00758-7

Heritage Science

RESEARCH

Open Access

Scientific investigation to look into the conservation history of a Tang Dynasty terracotta Dancing Horse

C. Conti[1*], M. Catrambone[1], C. Colombo[1], E. Possenti[1], K. M. Rectenwald[2], M. Realini[1] and P. Strobbia[3*]

Abstract

A terracotta Dancing Horse sculpture dating to the Tang Dynasty (China) and owned by the Cincinnati Art Museum (US) is the topic of the present investigation. Besides its intrinsic artistic and historical values, the peculiarity of this horse concerns its conservation history; it shows extensive breakage signs and restoration and above all, the presence of an odd tassel on the frontal part of the head. Nine tassels are present on the two sides of the body, which is very common for these kinds of sculptures. Here, a scientific survey of this masterpiece is proposed aimed at looking into its conservation history, shedding light into the condition of the body and the tassels and the presence of residual conservation products applied during its troubled history. A comparative molecular, chemical and mineralogical study of the tassels is carried out focused on the identification of original and non-original materials, eventually added during restoration works. The multi-analytical protocol has been optimized for achieving as much information as possible from the available samples, a few mg of powders. X-ray powder diffraction and Raman Spectroscopy techniques have been followed by Fourier Transformed Infrared Spectroscopy and Ionic Chromatography, using the same small aliquot of powders. Scientific investigations highlighted that the odd tassel on the head and other two tassels on the body are not original, but replaced or added in subsequent time. Their composition includes both organic (polyester resin and/or phthalate) and inorganic compounds (sulphates and carbonates). Further data on original terracotta composition, decay substances and applied conservation products, provided new knowledge on past restoration treatments and cultural value. Importantly, the outcomes achieved with X-ray powder diffraction to identify the tassels authenticity were matched by Raman Spectroscopy, a technique that can be also used in situ with portable instruments, paving the way to non-invasive in situ authenticity studies as future perspective.

Keywords: Tang Dynasty terracotta Dancing Horse, Multi-analytical approach, Conservation history, Authenticity, X-ray powder diffraction, Raman and Infrared spectroscopies, Ionic Chromatography

Introduction

The Tang Dynasty dancing horse terracotta sculpture was donated to the Cincinnati Art Museum in 1997 by a local private collector. The ceramic sculpture (H. 66 cm L. 61 cm W. 28 cm) is posed with one of the front legs raised and leaning slightly back on its hind legs, as if prancing. The horse has a knotted tail and saddle with nine tassel ornaments spaced along its body, likely molded separately and attached to the body before being fired. Traces of polychrome remain on the surface, though much has been lost. The horse stands on a ceramic base that is mounted to a wooden platform. Thermoluminescence conducted at the Research Laboratory for Archaeology and the History of Art at Oxford University (unpublished results, September 7th 1989 report), confirms that it was

*Correspondence: claudia.conti@cnr.it; strobbpo@ucmail.uc.edu

[1] Institute of Heritage Science (ISPC), National Research Council (CNR), Via Cozzi 53, 20125 Milano, Italy
[3] Department of Chemistry, University of Cincinnati, 312 College Dr., Cincinnati, USA
Full list of author information is available at the end of the article

last fired 800–1300 years ago, placing it within the Tang Dynasty.

Comparable horse sculptures, both unglazed and glazed, have been found in the tomb of high-ranking military general, Zhang Shigui (657 A.D.). A similar unglazed sculpture from the excavation of this tomb exists in the Shaanxi Provincial Museum [1]. Two other examples of similar unglazed horse sculptures that feature tassels exist in the Seattle Art Museum Collection (seventh-eighth century) and the Museum of Fine Arts Boston (first half of sixth century A.D.).

The peculiarity of the Tang Dynasty dancing horse of the Cincinnati Art Museum is the presence of an odd placement of the tassel on the forehead of the horse. The placement is unusual and is paired with an odd bare area on the body of the horse above the standing leg where, consistent with the tassel pattern around the body, it appears that a tassel is missing. These unusual areas raised questions about whether the placement of the tassels on the body of the sculpture were original. When examining the tassels under UV light, adhesive can be seen around the edges of many of the tassels indicating that restoration has occurred at some point in the past. To determine whether the tassels are attached in their original locations, an understanding of the past condition and conservation history of the sculpture is essential.

Museum records indicate that prior to the donation, the sculpture was recorded as having been broken and restored in 1990. Unfortunately, the museum retains no photos of the sculpture before the damage, no records of the extent of the damage, and no records of the restoration that followed. Fortunately, Cincinnati Art Museum does have records from a 2006 conservation treatment carried out by conservators at the museum. During this treatment the conservator notes the presence of extensive overpaint and plaster fills which cover parts of the original surface. The 2006 report, supported by recent examination, indicates that under UV light, much of what appears to be archaeological surface dirt, is present over plaster fills and overpaint and is a modern addition to disguise the old repairs. To aid in understanding the extent of treatments prior to 2006, partial X-rays were taken (Additional file 1: Fig. S1). These revealed that the sculpture had extensive breaks with dowel rods placed at many of the joins, including the neck, legs, and tail. This evidence indicates that the sculpture suffered from extensive damage and restoration prior to entering the museum, some from the 1990 treatment organized by the previous owner, but it is also possible that the horse had been broken during burial and repaired prior to the private owner's purchase.

With no existing records of the condition or treatment prior to entering the museum, it is difficult to establish what has changed and how the "original" may have appeared. Much of the 2006 conservation treatment was aimed at reducing the extensive restoration materials present to reveal more of the original surface. Still, where most of the tassels meet with the body of the horse, adhesive and fill materials can be seen in visible and UV light. Due to the unusual placement of the tassel on the head and the absence of a tassel on the body of the horse, paired with our knowledge that undocumented restoration occurred, we question whether the placement of all of the tassels is original. To understand whether the forehead tassel is indeed misplaced, more analysis is needed.

Usually, historical and artistic studies of terracotta materials are complemented by petrographic, mineralogical and chemical analyses [2]. A multi analytical approach is required [3–5] mainly including Inductively Coupled Plasma-Mass Spectrometry (ICP-MS) [6] and X-ray Fluorescence (XRF) to provide insights into the provenance of materials, polarized optical microscopy (POM), Energy Dispersive X-ray Spectroscopy (EDS) and X-ray diffraction (XRD)[7] to study the entire manufacturing process, including heating conditions such as firing temperature and atmosphere. Vibrational spectroscopy methods (Fourier Transformed Infrared and Raman Spectroscopies) are also recently adopted [6, 8] for the same purpose.

Therefore, it was decided that very small samples of each tassel as well as the main body could be taken for scientific analysis, aimed at characterizing their composition. The main purpose is to identify restoration materials and possible unoriginal parts, matching the tassel composition with that of the main horse body. Answering these questions will aid in decision making surrounding the next treatment of the sculpture. The analytical challenge faced here consists in the development of the best multi analytical approach able to extract as much information as possible from the small amount of available powdered sample (a few mg). First, selected methods have been used non-destructively and sequentially on the same powders; then, chemical treatments have been applied to the powders and further measurements carried out also with micro-destructive methods. The overall outcomes achieved with X-ray powder diffraction (XRPD), Ionic Chromatography (IC), Raman Spectroscopy (RS) and Fourier Transformed Infrared spectroscopy (FTIR) allowed providing insights about mineralogical, chemical and molecular composition of the samples, shining a light on the firing technology, past conservation treatments and decay as well as on the tassels authenticity.

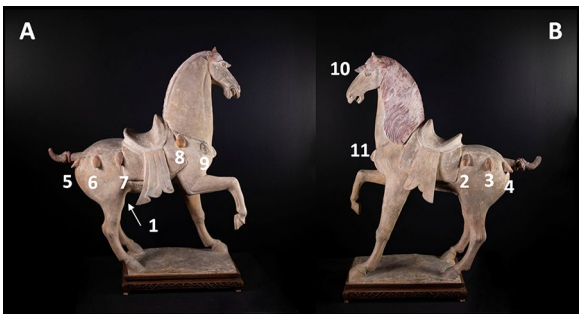

Fig. 1 Images of the right (**a**) and of the left (**b**) sides of the terracotta horse (H. 66 cm L. 61 cm W. 28 cm). Dancing Horse, 608–907 CE, China, Tang Dynasty, earthenware with pigments, Cincinnati Art Museum, Gift of Carl and Eleanor Strauss, 1997.53

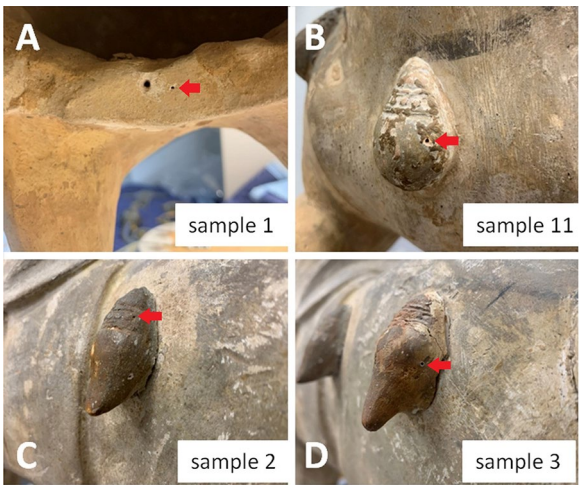

Fig. 2 Sampling points indicated by the red arrows of sample 1, inside the abdomen cavity (**a**), sample 11, from one of the frontal tassels where remains of white and ochreous finishing layers are visible (**b**), sample 2 where brown layer is present (**c**), sample 3, where adhesives are visible between tassel and horse body

Materials

In Fig. 1 and Additional file 1: Table S1 the samples labels and their location on the horse are reported. The tassels were sampled in the top portion and drilled through with a 0.8 mm steel drill bit to a depth of 5 mm; this provided a sample of mixed layers that are not isolated from each other. All the samples have been taken from the tassels, except for sample 1 which results from the interior part of the horse, inside the cavity located in the abdomen (Fig. 2a). The weight of the samples ranges from 2.9 to 9.7 mg.

The visual inspection allows identifying several remains of white and ochreous finishing layers both on the tassels and on the horse body (Fig. 2b). Moreover, an external and homogeneous brown layer is present in most of the tassel surfaces (Fig. 2c).

Methods

To maximize the analyses of the samples, the following analytical protocol has been planned considering the possibility to reuse the same powders for different analytical techniques measurements. First X-ray powder diffraction (XRPD) and Raman Spectroscopy (RS) have been carried out: the powders are deposited on the sample holder and analyzed without any pre-treatment. Then, Fourier Transformed Infrared spectroscopy (FTIR) and Ionic Chromatography (IC), that need a sample preparation before the analysis, have been performed; at first, a small aliquot of powders (~1 mg) was micro sampled for preparing KBr pellets. The remaining powders were used for ionic chromatography analysis; after IC, the solutions left over were dried and the resulting insoluble powders were re-used for FTIR analyses using the solvent extractions.

X-ray powder diffraction (XRPD)

A Panalytical X'Pert PRO X-ray powder diffractometer was used to identify the crystalline composition of the powders. The instrument equipped with a X'Celerator detector PW3015/20 and diffraction patterns have been collected from 5° to 60° 2θ, scan speed 0.21°/sec, with a CuKα-radiation source, working conditions 40 kV and 40 mA. Powdered samples have been spread on an amorphous silicon holder and then analysed. X'Pert Highscore software was used to aid XRD spectra interpretation.

Raman spectroscopy (RS)

Raman spectra of the powder samples were collected using an InVia Raman microscope (Renishaw) using a 785 nm laser (Innovative Photonic Solutions) at a 50% power (nominal laser power is 200 mW). The objective used was a 50X (Leica). The spectra were recorded with a total exposure time of 10 s and each sample was measured in 9 different points. The baseline was subtracted using a Savitzky-Golay filter (five-point window) written by the laboratory of Department of Chemistry, University of Cincinnati, on MATLAB.

Fourier transformed infrared spectroscopy (FTIR)

FTIR investigations were carried out by a Thermo Scientific™ Nicolet™ Nexus spectrophotometer (DTGS detector) coupled with a Continuμm™ infrared microscope (15 × objective) equipped with an MCT/A detector cooled with liquid nitrogen. The samples were divided in different aliquots to be analysed in transmission with two different instrumental setups.

First, KBr pellets (~1 mg sample: 120 mg KBr) were analysed in the optical bench to study the vibrational

features of organic and inorganic compounds over the full mid infrared spectral range (4000–400 cm^{-1}).

Then, solvent extractions were carried out to highlight the presence of organic substances and study their composition. The samples were immersed in two solvents having different polarity (dimethyl ketone, hexane; both of them spectroscopic grade, assay ≥ 99.9%) for 2 h at room temperature in sealed vials to extract the soluble fraction. Then, the solution was sampled by using a pipette, dropped on watch glasses and dried 24 h at room temperature under ventilated fume hood to ensure the complete evaporation of the solvents. No solid residues were individuated after hexane extraction. The solid residue obtained by dimethyl ketone was micro-sampled and placed on a diamond anvil cell to be analysed by FTIR (spectral range 4000–650 cm^{-1}, investigated area 100×100 μm^2).

The FTIR spectra were collected with a spectral resolution of 4 cm^{-1} and 128 co-added scans. The software Omnic 9 was used to collect the FTIR patterns. The spectra are shown without any spectral manipulation.

Ionic chromatography (IC)

Before the analysis, the samples were dried for 24 h in oven at 60°C and weighed using microbalance (Sartorius). Dry weights varied between 0.77 and 7.5 mg. Each sample was put into 8 ml vial containing deionized water (3 ml) then shaken by mechanical shaker for 2 h for complete extraction of the ionic compounds.

The solution was then filtered through a 0.45 µm filter and analysed by ion chromatography (IC). The analysis was carried out by ICS1000 (Thermo Fisher). Cations (Na^+, NH_4^+, K^+ Mg^{2+} and Ca^{2+}) were determined by column ION PAC CS12A-4 mm, pre-column ION PAC CG12A-4 mm and CSRS-ULTRA-4 mm suppressor. Methanesulphonic acid, in isocratic mode, was used as eluent (20 mM, flow rate of 1.2 ml/min). Anions (Cl^-, NO_2^-, NO_3^-, CO_3^{2-}, SO_4^{2-}, $C_2O_4^{2-}$ and PO_4^{3-}) were determined by column AS11-4 mm, pre-column AG11-4 mm and ASRS-ULTRA 4 mm suppressor. Potassium Hydroxide, generated by ECG40 EGC II KOH (Thermo Fisher) in gradient mode (from 10 up to 60 mM) was used as eluent.

Results

First, the outcomes achieved by the single techniques are presented; then, a full overview of the analytical investigation has been proposed in the "Discussion" paragraph. Due to their complementarities and vibrational spectroscopy nature, Raman and FTIR are presented in the same paragraph.

X-ray diffraction

X-ray diffraction patterns have been analyzed both qualitatively, for the identification of the crystalline phases, and semi-quantitatively for estimating their relative ratio percentages. The latter analysis has been carried out assigning hundred per cent value to the intensity of the most intense peak, and calculating the relative intensity percentage of the other peaks. The results have been plotted in the ternary diagram (Fig. 3), where a selection of the most significant crystalline phases is proposed on the basis of the following considerations: a noticeable number of samples show a high content of quartz (SiO_2); phyllosilicates (talc—$Mg_3Si_4O_{10}(OH)_2$, phlogopite—$KMg_3(Si_3Al)O_{10}(F,OH)_2$ and sericite $KAl_2(AlSi_3O_{10})(OH)_2$ clay minerals) are a further representative group of minerals; the non-silicatic group exhibits relevant amount of carbonates (calcite $CaCO_3$, dolomite $CaMg(CO_3)_2$, magnesite ($MgCO_3$)) and sulphates (gypsum $CaSO_4 \cdot 2(H_2O)$). For a sake of completeness, other minor amount of silicates as feldspars (orthoclase $KAlSi_3O_8$, albite $NaAlSi_3O_8$, plagioclase $(Na,Ca)(Si,Al)_4O_8$) and mullite ($Al_6Si_2O_{13}$) are added to the quartz values.

As shown in Fig. 3, the main outcome is the presence of a major cluster of samples (1–4, 6–7, 9, 11) with a high amount of one or more minerals included in the quartz-feldspars-mullite group; considering also that these samples show the presence of phyllosilicates (Fig. 4 and Additional file 1: Table S2), it is reasonable to ascribe this cluster to terracotta materials; the presence of hematite (Fe_2O_3) in two samples further supports that. Actually, a deeper look allows noticing that sample 1 differs from the others because mullite is present (Fig. 4 and Additional file 1: Fig. S2). This mineral is meaningful for exploring the terracotta firing process; it is well known [9] that sericite-illite clays used for producing terracotta wares

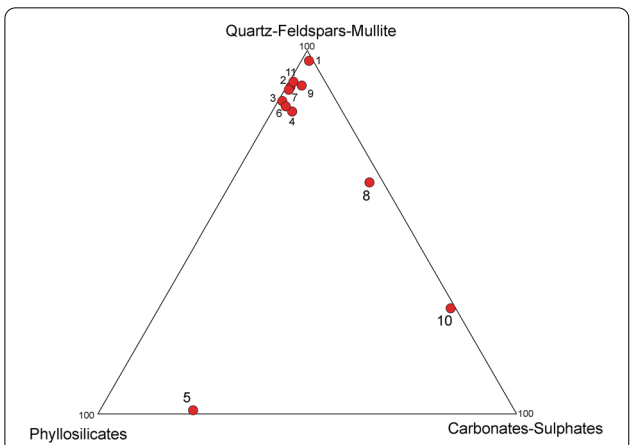

Fig. 3 Ternary diagram representing XRD data. The sample labels are indicated close to the dots

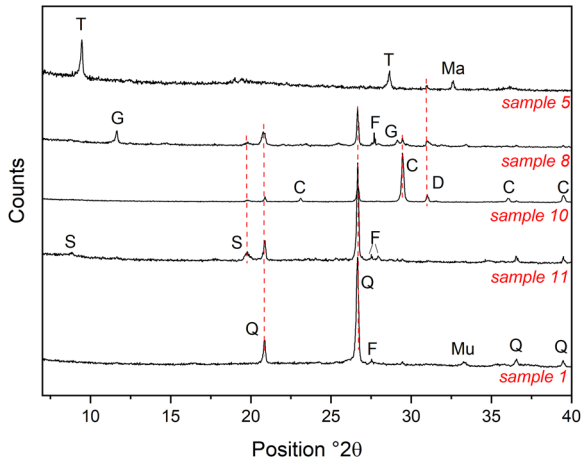

Fig. 4 XRD spectra of selected samples, representative of the entire sample set. Q: quartz, F: feldspars, Mu: mullite, S: sericites, C: calcite, D: dolomite, G: gypsum, Ma: magnesite, T: talc

undergo mineralogical changes at specific heating temperatures. First, clays lose "free moisture", mechanically retained or adsorbed water, in the range between 50 and 200 °C. At higher temperature, in the range 400–800 °C, a dehydroxylation of the clay minerals occurs, due to the water elimination of structural OH groups of the layered structures. Sericite clay minerals starts changing into the dehydroxylated phase [$KAl_2(AlSiO_3)O_{11}$] at about 500 °C; however, many factors influence this process and literature reports different temperature ranges [10, 11], indicating that the maximum range is 850–1000 °C. The increase of firing temperature induces a breakdown of the dehydroxylated sericite-illite phase, with a consequent formation of mullite at about 1050 °C. Based on this thermal behavior, the firing temperature of the above samples can be inferred: tassels number 3, 4, 6, 7, 9 and 11, showing a relevant amount of sericites and phlogopite, have been fired below 900–1000 °C whereas sample 1, which exhibits mullite, over 1050 °C; however, the absence of quartz polymorphs in sample 1 points out that it does not exceed 1200 °C [12, 13].

It is worth highlighting that samples seem to derive from the same clay paste made by a non-calcareous clay, as demonstrated by the lack of the firing transformation minerals of calcareous clays as gehlenite and diopside, and the presence of mullite; moreover, the same source is also confirmed by the presence of sericite-illite clay minerals in all samples (except for sample 1 that has been fired at higher temperature, with a consequent collapse of sericite-illite crystalline structure). Based on these results, the low quantity of calcite detected in some samples of this terracotta cluster (4, 6, and 9) cannot be attributed to the terracotta original composition, but it could point out to burial conditions to which the horse could have been subjected; during the burial time, a secondary crystallization of calcite may have occurred. A further explanation of calcite source can be found in the residual of applied finishing layers or of conservation products made with an inorganic matrix.

A distinction is made for samples 5, 8 and 10 which deserve independent discussion due to their particular position in the ternary diagram. XRD spectrum of samples 5 exhibits high background and significant degree of noise, indicating the presence of amorphous compounds which cannot be identified with this technique. Over this background, the main characteristic peaks of talc, magnesite and dolomite can be distinguished (Fig. 4 and Additional file 1: Fig. S2). No reasonable hypothesis can be formulated about the nature of this tassel based on XRD data only.

Sample 8 comprises a high relative content of carbonates and sulphates, despite the main mineral is quartz, and little amount of sericite clay minerals (Fig. 4 and Additional file 1: Fig. S2). The main mineral of sample 10 is calcite; dolomite, quartz and sericites are also detected (Fig. 4 and Additional file 1: Fig. S2). Looking at the mineralogical composition of these three tassels (samples 5, 8 and 10), it is apparent that they cannot be included in the terracotta group; as for 8 and 10, their relative high amount of carbonates (and sulphates in sample 8) points out a stucco material, prepared with a carbonate/sulphate matrix and silicates as aggregate.

Nitratine ($NaNO_3$), detected in five samples, attests a certain degree of decay, which is further studied through the following analyses, in particular with ionic chromatography.

Vibrational Spectroscopy: Raman and FTIR

Raman spectra acquired on the same powders confirmed XRD outcomes and provided additional data. Due to its high Raman scattering cross section, anatase (TiO_2) has been detected in almost all the samples (Fig. 5a, b), whereas in XRD spectra just a very weak, and in some cases negligible peak, is present. In art objects, anatase could be ascribed to two different sources: it can be associated to silicates or oxides as accessory mineral, or it indicates the presence of a finishing layer made by titanium white (rutile and/or anatase), a white pigment widely used since nearly 1920.

One of the main advantages of micro-Raman includes the possibility to observe the powdered samples with a microscope objective and accurately select the grains to be analyzed, correlating their color to a specific composition. This is the reason why hematite (Fe_2O_3) has been frequently identified by Raman (Fig. 5a), especially in terracotta samples, thanks to its red color. Only in some

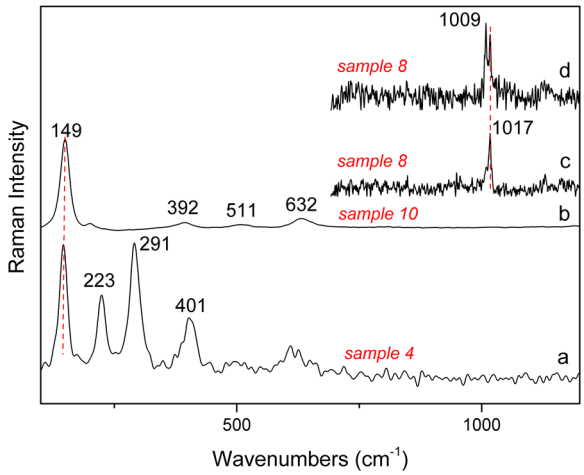

Fig 5 Selected and representative Raman spectra where **a** hematite (223, 291, 401 cm^{-1}) and anatase (149 cm^{-1}), **b** anatase (149, 392, 511, 632 cm^{-1}), **c** anhydrite (1017 cm^{-1}), **d** anhydrite (1017 cm^{-1}) and gypsum (1009 cm^{-1}) were detected. **c**, **d** spectra are acquired in two different areas of the sample 8 powder

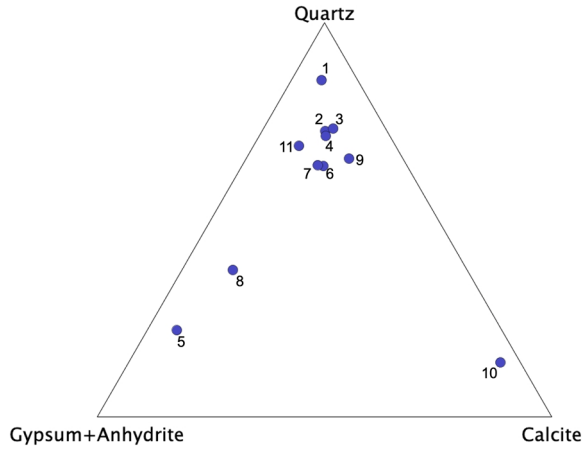

Fig. 6 Ternary diagram representing Raman data. The sample labels are indicated close to the dots

XRD spectra a weak hematite peak is visible, confirming that micro-Raman is the technique of choice when colored particles are present in a mixture in low quantity. Hematite is a frequent mineral in terracotta materials, demonstrating the transformation of iron phases in oxidizing firing conditions. It provides the typical red color to the matrix, and tiny amount is enough to give this coloration. However, the employment of red ochre (hematite) in finishing layers cannot be completely excluded.

XRD results revealed that sample 8 has the highest relative amount of gypsum. Micro-Raman analysis of this sample allowed noticing the presence of anhydrite ($CaSO_4$) in mixture with gypsum (Fig. 5c, d). Anhydrite is the anhydrous calcium sulphate form, not easily detectable by XRD due to severe peaks overlapping. Its presence could demonstrate a decay of the stucco as gypsum loses its water molecules at temperatures above 30 °C-40°C and moderate R.H. (30–40%), with a consequent crystallization into anhydrite [14]. Alternatively, anhydrite could indicate a calcination of the gypsum rock at high temperatures; this process is aimed at increasing the mechanical characteristics of the stucco, as anhydrite needs less kneading water [15].

The contribution of the characteristic peaks of the main minerals present in the Raman spectra of the samples has been plotted in a ternary diagram to perform a semi-quantitative analysis of the data. The ternary diagram is based on the Raman bands for quartz at 464 cm^{-1}, gypsum at 1009 cm^{-1} and calcite at 1087 cm^{-1}. The reported values represent the integral under the curve of the peak and was normalized to the sum of all three peaks, or spectral region in the absence of the peak. The peak for anhydrite (1017 cm^{-1}) was also added to the gypsum peak. As it can be observed in Fig. 6, sample 1 (the reference from the body of the horse) showed the highest quartz concentration as expected and as seen in XRD data. Most of the tassels (samples 2–4, 6–9, 11) clustered at high concentration of quartz, while samples 5, 8 and 10 were outliers. Sample 10 had a high value for the calcite axis and sample 5 and 8 instead had a high value for the gypsum and anhydrite axis.

Information about organic compounds have been achieved by Raman in sample 5. As mentioned above, XRD spectrum suggested the presence of an amorphous compound; some characteristic bands of organic compounds have been observed in the Raman spectrum, as reported in Fig. 7. An interesting result has been achieved coupling Raman and FTIR data: besides talc (3677 cm^{-1}, 1019 cm^{-1} and 670 cm^{-1} in FTIR spectrum) and low amount of dolomite, a synthetic polymer is unequivocally identified through the bands at 1726 cm^{-1}, 1494 cm^{-1}, 1271 cm^{-1}, 1122 cm^{-1} in the FITR spectrum and 1000 cm^{-1}, 1045 cm^{-1}, 1605 cm^{-1} and 1732 cm^{-1} in the Raman spectrum, suggesting the presence of a polyester resin and/or a phthalate.

FTIR analyses have been focused on the identification of organic components within the sample powders, through the extractions with dimethyl ketone. In Fig. 8 four representative FTIR spectra of compounds detected in the samples after the solvent extraction are reported; cellulose nitrate (CN) is clearly identified by the characteristic vibrations at 1656 cm^{-1}, at 1280 cm^{-1} and ~ 840 cm^{-1} of nitrate groups ($\nu_{as}NO_2$, $\nu_{as}NO_2$ and $\nu O\text{-}NO_2$, respectively; FTIR spectrum of sample 8 in Fig. 8). The cellulosic vibrational envelope between

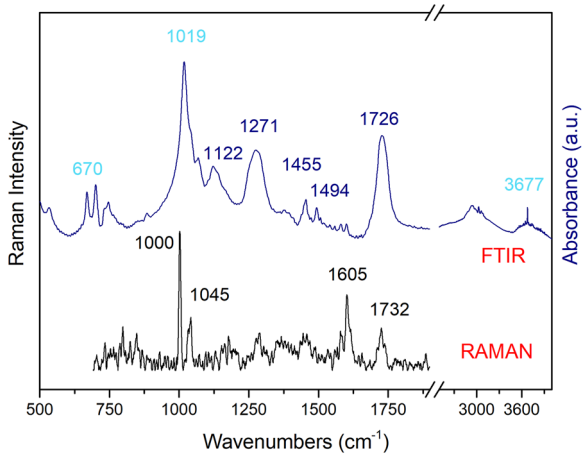

Fig. 7 Raman and FTIR spectra acquired on sample 5. FTIR spectrum shows the vibrational pattern of both talc (light blue wavenumbers) and polyester resin and/or a phthalate (dark blue wavenumbers). Raman spectrum shows the band of polyester resin and/or a phthalate

1220–840 cm^{-1}, with the strong COC stretching vibration at 1077 cm^{-1}, confirms the detection of cellulose nitrate in several samples (2,-4,6–8,10–11) [16, 17].

Moreover, other organic substances are in mixture with cellulose nitrate; in sample 6, an acrylic resin is inferred by the strong band at 1730 cm^{-1} ($\nu C=O_{ester}$), by the vibrational modes at 2959 cm^{-1}, 2926 cm^{-1}, 2874 cm^{-1}, 2854 cm^{-1} (νCH_3 and νCH_2) as well as by the characteristic bands in the fingerprint region at 1453 cm^{-1}, 1389 cm^{-1} (in-plane δ_{as} and δ_{sy} of C–H), at 1240 cm^{-1}, 1027 cm^{-1} ($\nu C–O_{ester}$), 1151 cm^{-1} (out-of-plane δ C–H) and 749 cm^{-1} ($\delta_{rocking}–CH_2–$) [18].

In samples 1, 3, 4, 7, 10 and 11 a weak absorbance band at 1730 cm^{-1} is ascribable to an acrylic resin in very low amount. On the other side, this peak could also be attributed to camphor, a plasticizer commonly used to stabilize CN, albeit the C=O stretching vibration of camphor is in general at higher wavenumbers [16]. Therefore, in samples 1 and 9, where cellulose nitrate has not been detected, this band has to be ascribed to an acrylic resin; in the other samples the presence of an acrylic resin in mixture with cellulose nitrate cannot be excluded.

Proteins, in very low amount, could be present in samples 3, 4, 7 and 10 as suggested by the absorption bands at 3344 cm^{-1}, 3077 cm^{-1}, 1656 cm^{-1} and 1537 cm^{-1} attributed to the νN-H, amide I and amide II vibrational modes [19, 20]. A further organic substance, having a peak at 1713 cm^{-1} is identified in samples 2, 8 and 11 (see FTIR spectrum of sample 2 in Fig. 8). This absorption band is due to the C=O stretching and is compatible with an organic acid, most likely released by degraded organic polymers in the samples. In addition, the presence of nitrates (837, 1371 cm^{-1}) and OH stretching broad bands (between 3650–3200 cm^{-1}) after the solvent extraction of all the samples containing cellulose nitrate can be correlated to the decay of CN via hydrolysis [21, 22]. In all the spectra of extracted samples, the strong bands at 2959, 2926, 2874, 2854 cm^{-1} are due to the symmetric and asymmetric stretching of CH_2 and CH_3 groups. Considering the sharp shape of these bands and their position, they could be attributed to an aliphatic compound, most likely a paraffin or a wax.

The inorganic phases identified by FTIR perfectly fit with XRD data, identifying a main group composed by samples 1, 2, 4, 6, 7, 11, dominated by the vibrational modes originating from quartz and other hydrated silicates (S2) and three samples (10, 8 and 5) showing different features. Sample 10 is significantly different since its FTIR spectrum mainly shows the vibrational bands of calcite; moreover, nitratine $NaNO_3$ (1385 cm^{-1}, 837 cm^{-1}) is unequivocally detected. According with XRD data, gypsum is one of the most relevant phases in sample 8, in mixture with quartz.

Ionic chromatography

The samples showed a high variability of the solubility in water. The mass fraction of water-soluble ions (WSI), with respect to the total mass of sample, ranges from 1.0% (sample 1) to 34% (sample 8).

The ionic composition (sum of anions and cations) as percentage of each sample, is shown in Fig. 9.

The prevailing anion was SO_4^{2-} followed by NO_3^-. On average, SO_4^{2-} and NO_3^-accounted for 60% and 2.9%, respectively, of the total ions mass. The prevailing cation was Ca^{2+} followed by K^+. On average, Ca^{2+} and K^+ accounted for 29% and 1.0%, respectively, of total ions mass.

Good correlations ($R^2=0.844$) between anion and cation μEquivalents (μEq) (Additional file 1: Fig. S3) were found for all samples except for the samples 1, 3 and 10; deficiency of cations in sample 3, deficiency of anions in sample 1 and 10. In Additional file 1: Fig. S4 a strong correlation ($R^2=0.998$) is obtained removing samples 1, 3 and 10.

The scatter plots of SO_4^{2-} versus Ca^{2+}, SO_4^{2-} versus CO_3^{2-}, NO_3^-versus Cl^- and NO_3^- versus Na^+ are depicted in Fig. 10. Strong correlation between SO_4^{2-} and Ca^{2+} was found ($R^2=0.974$) (Fig. 10a) suggesting the presence of $CaSO_4$ (most likely gypsum) in all samples, with the exception of sample 10. The high sensitivity of ionic chromatography is demonstrated by the detection of calcium sulphate even in samples where XRD does not show any evidence.

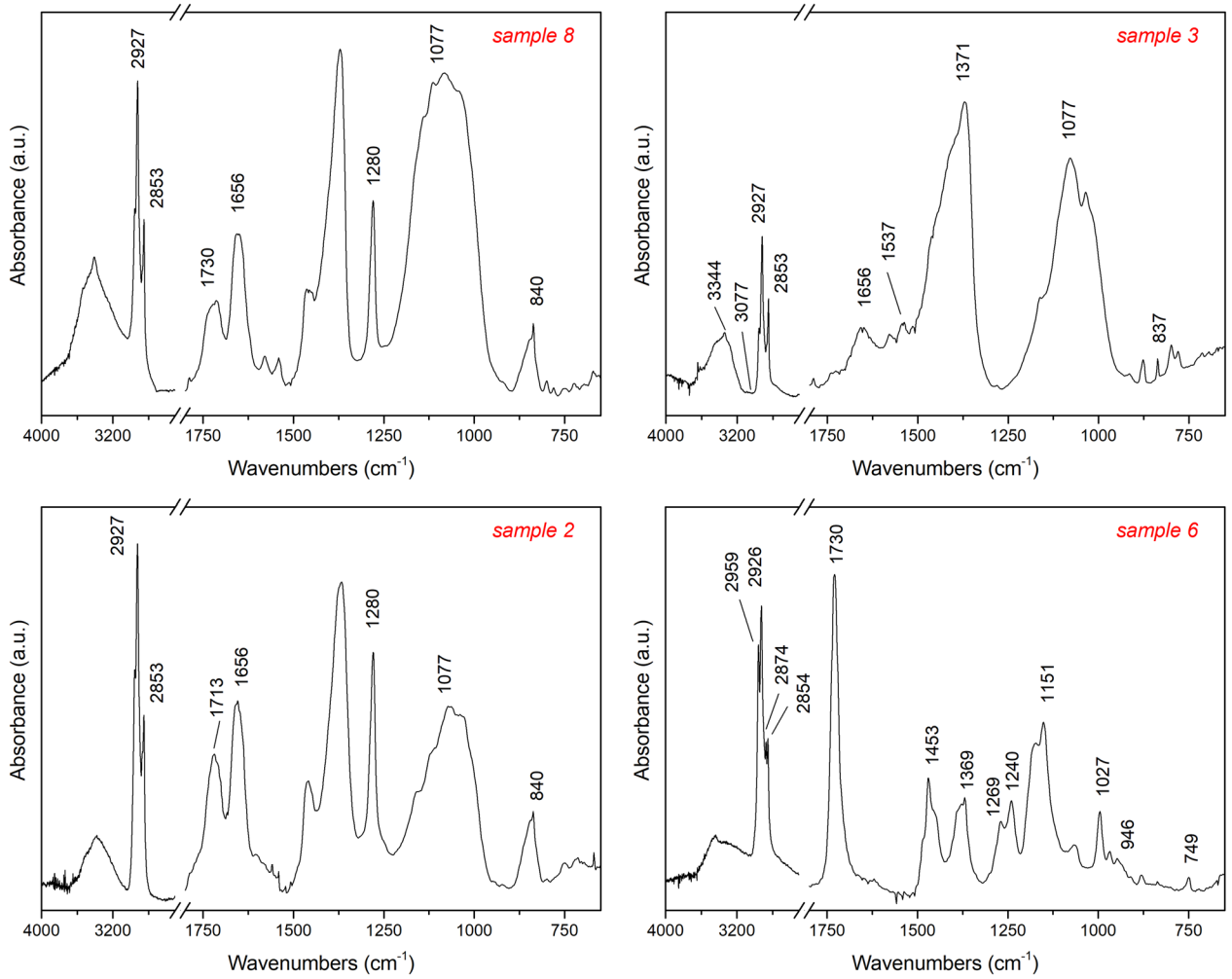

Fig. 8 FTIR spectra collected in transmission on diamond anvil cell of the solid residue obtained after extraction with dimethyl ketone of samples 8, 2, 3 and 6

The relation of sulphate and carbonate shows that in some samples (green circle in Fig. 10b) high value of sulphate corresponds to low value of carbonate. This could be explained considering the degradation of calcite and the consequent formation of gypsum [23], despite here any analytical evidence has been found for supporting this hypothesis.

A good correlation was observed (Fig. 10c) for nitrate and chloride (R2 = 0.858), whereas weak correlation was observed for nitrate and sodium (Fig. 10d). In two samples (sample 3 and 10) the ratio NO_3^-/Na^+ was higher (11 and 8.6, respectively) with respect to other samples (average ratio 1.5). Sample 3 is the only one with an excess of anions; however, in this sample sulphate was almost totally neutralized by calcium (strong correlation sulphate vs calcium), and nitrate was 11% by weight; considering that nitrate cellulose (CN) was observed in almost all samples by FTIR, the hydrolysis and subsequently degradation of CN [16, 24] could be suggested with a consequent enhancement of solubility of nitrate.

Anion deficiency was observed in samples 1 and 10 which is more likely due to the fact that HCO_3^- and organic acid are not detected by IC; moreover, a release of HNO_2, HNO_3, and CH_3COOH as a consequence of degradation of CN [16] cannot be excluded.

The presence of oxalate in all samples could indicate the mineralization of organic compounds as well as the CN nitrate scission [16].

Discussions

A critical overlook over the entire set of outcomes achieved by the applied multi-analytical approach allows shading light on the following aspects:

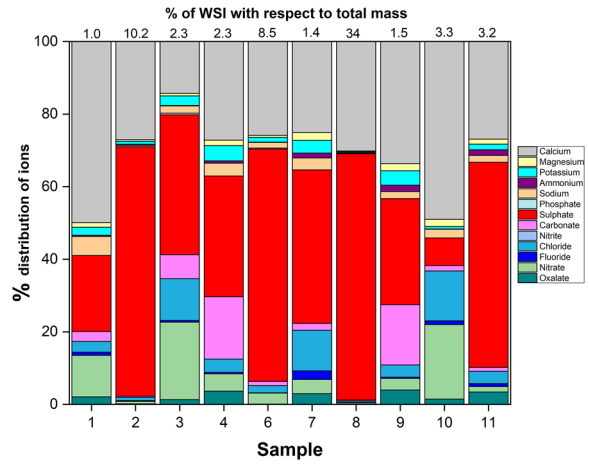

Fig. 9 Percentage distribution of WSI in the samples (the columns show colours as reported in the legend on the right). The percentage of WSI with respect to the total mass is reported on top of the figure

Tassels composition

We suggest that most of the tassels (samples 2, 3, 4, 6, 7, 9 and 11) have been applied to the horse at the time of its manufacturing, whereas tassels 5, 8 and 10 have been replaced or added in subsequent different periods. This hypothesis is supported by the compositional similarities of samples 2, 3, 4, 6, 7, 9 and 11 to each other and their consistency with sample 1, which is likely original. A non-carbonatic clay has been fired with oxidizing conditions below 900–1000 °C (samples 2, 3, 4, 6, 7, 9 and 11) and in the range between 1050 and 1200 °C (sample 1).

Samples 5, 8 and 10 are not made of terracotta, as also suggested by the visual inspection (Fig. 11); due to the compositional differences among the three tassels, we can also suggest that they have been applied to the horse separately, namely in three different restoration actions; in fact, three kinds of binders have been employed: polyester resin and/or a phthalate in sample 5, sulphates and carbonates in sample 8 and carbonates in sample 10. Samples 8 and 10 contain sericites clay minerals, indicating a contamination of the surrounding original materials during the drilled sampling.

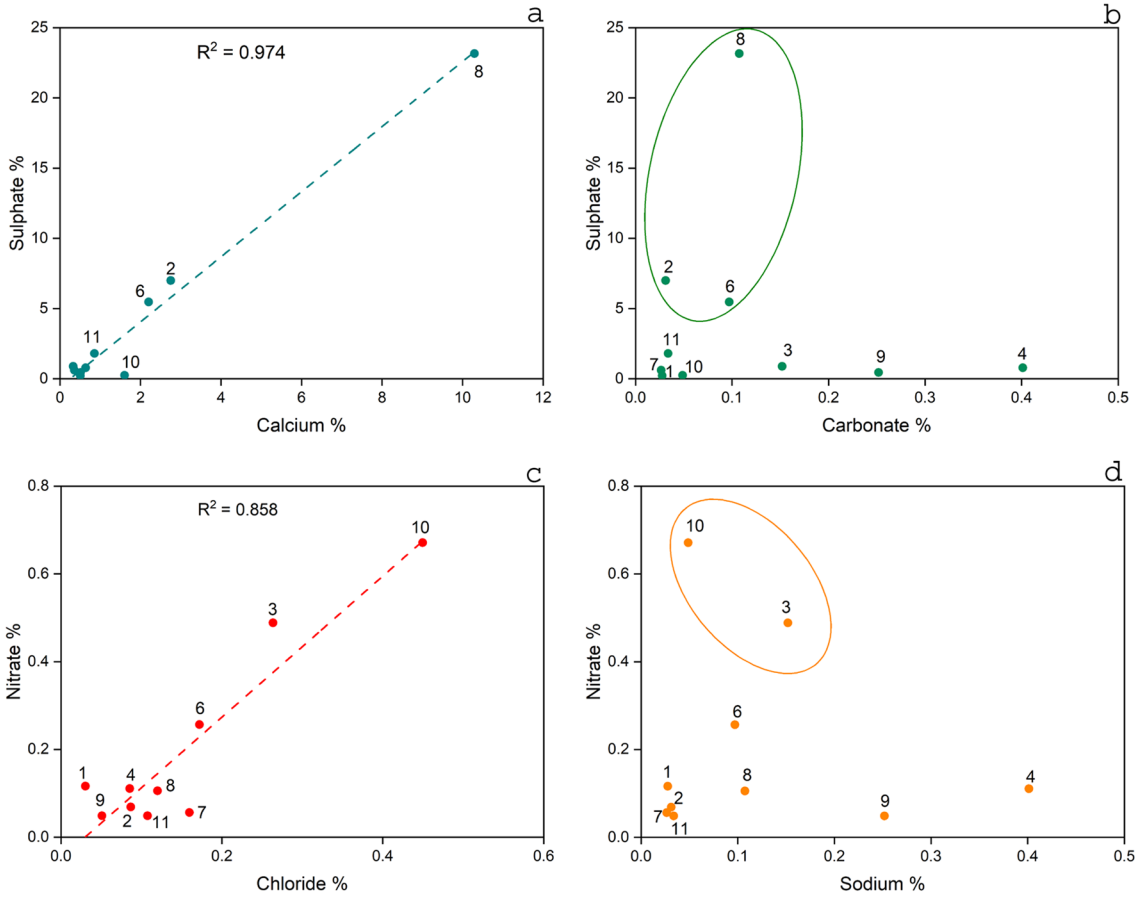

Fig. 10 Scatter plots of different ions: **a** SO_4^{2-} vs Ca^{2+} **b** SO_4^{2-} vs CO_3^{2-}; **c** NO_3^- vs Cl^- and **d** NO_3^- vs Na^+

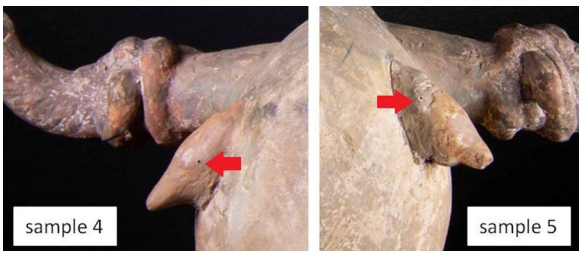

Fig. 11 Sample 4, representative of terracotta tassels (left) and sample 5, one of the stucco tassel (right). The red arrows indicate the sampling points

External layers

A visual inspection of the horse allows for a good assessment of the condition of both the body and the tassels. Organic materials as adhesives and/or fixatives are visible at the connection area between the base of the tassels and the body, indicating that the horse has been subjected to extensive restoration during its history (Fig. 2d). Moreover, several remains of finishing layers have been observed on the tassels surfaces showing a critical conservation state; the layers are overlapped one on top of each other, and the visual inspection suggests the presence of a white layer over the ceramic substrate, followed by an ochreous layer. Based on these evidences, calcium sulphate, that is present in all the samples except for the sample collected from the tassel of the head, calcite, anatase and hematite can be ascribed to the inorganic portion of the finishing layers; hematite can also influence the color of the ochreous layer. The horse has been likely subjected to burial conditions, thus calcite and gypsum can also be ascribed to the resulting decay products.

A brown organic homogeneous layer has been observed on several tassels; FTIR allowed identifying at least three organic compounds related to conservation products, demonstrating interventive conservation treatments to the horse during its life. Nitrocellulose, detected both in some terracotta and stuccoes tassels, is related to synthetic resins or varnishes applied extensively on the tassel surface. Acrylic resin is commonly used in conservation as a coating or adhesive; proteins represent a high number of different products as glues used as adhesives.

A decay of the nitrocellulose has been pointed out; the hydrolysis mechanism of this compounds leads to an increase of nitrate solubility. To the best of our knowledge, for the first time ionic chromatography provides evidence of conservation product decay, opening the way to a new application of this method in the heritage science. Other decay products as nitratine, that could be originated as a secondary product of conservation treatments applied on the horse, and oxalates have been detected; the latter are present in all samples, likely indicating a mineralization of the organic substances, binders or conservation products as nitrocellulose.

Conclusions

Relevant indications on the horse history and its condition have been achieved using a few mg of powders and a multi-analytical approach focused on the identification of both inorganic and organic compounds. The maximization of the analyses results has been achieved planning the best analytical path able to use as much as possible the available powders. One of the most relevant result is that the odd tassel on the head and other two tassels on the body are not original but replaced or added in subsequent time.

These results, paired with the curatorial and conservation history, provided evidence to support the removal of the forehead tassel. It was attached to the body via a previous repair using animal glue, which was softened with low heat until the tassel released. Once the tassel was removed there was no evidence on the head, such as scoring, to indicate that there had ever been a clay attachment here. With visual examination of the detached tassel, at least two different materials could be seen. Plaster, which has been used at the top of the tassel to create a surface that allows it to conform to the forehead for attachment. Beneath the plaster a chalky grey material can be seen which has a completely different curvature that does not match the forehead of the horse, further supporting that this tassel was never originally positioned on the forehead.

Interestingly, XRD and Raman ternary diagrams show clustered vs outlier samples, answering the main questions regarding the authenticity of the tassels. Raman can also be used non-invasively and in situ, with portable instrumentation, making it ideal in conservation science. This study paves the way for the use of Raman in similar projects, giving material authentication answers to conservators directly at the museum.

The remaking of three tassels is one of most relevant outcomes highlighted by this scientific investigation. The identification of decay minerals and residual conservation products sheds light on the effect of the past treatments, that in some cases, produced secondary undesirable effects and provides to conservators essential information to plan future conservation treatments.

Abbreviations

ICP-MS: Inductively Coupled Plasma-Mass Spectrometry; XRF: X-ray Fluorescence; POM: Polarized optical microscopy; EDS: Energy Dispersive X-ray Spectroscopy; XRD: X-ray diffraction; XRPD: X-ray powder diffraction; IC: Ionic Chromatography; RS: Raman Spectroscopy; FTIR: Fourier Transformed Infrared spectroscopy; UV: Ultraviolet.

Supplementary Information

The online version contains supplementary material available at https://doi.org/10.1186/s40494-022-00758-7.

Additional file 1: Figure S1: montage of X-radiographs reveals extensive past alterations. There are many breaks in the mane, head, legs, lower saddle, and platform. Dowels can be seen in the legs, tail, and saddle. Figure S2: FTIR spectra collected in transmission on KBr pellets of samples 11 (i), 10 (ii) and 8 (iii). Sample 11 is dominated by quartz bands (1162, 1080, 1055, 799, 780 and 694 cm-1) and hydrated silicates (3630, 3549, 559, 510, 480 cm-1); sample 10 shows the bands of calcite (1428, 876, 713 cm-1) and nitratine (1385, 837 cm-1); sample 8 exhibits the vibrational modes of gypsum (3547, 3406, 1685, 1621, 1144, 1119, 670, 603 and 479 cm-1). Figure S3: Scatter plots of total anions vs. total cations (μEq) of each sample. Figure S4: Scatter plots of total anions vs. total cations (μEq) without samples 1, 3 and 10. Table S1: sample labels and their location. Table S2 : XRD results for each sample indicated in the left column.

Acknowledgements
Not applicable.

Author contributions
CC wrote introduction, XRD paragraph, discussions and conclusions, KR wrote the introduction and conclusions, EP wrote FTIR paragraph and discussions, MC wrote IC paragraph and discussions, MR wrote discussions and conclusions, CC wrote XRD paragraph, discussions and conclusions, PS wrote Raman paragraph, discussions and conclusions. Figures have been prepared by EP, CC, MC, CC and PS. All authors read and approved the final manuscript.

Funding
No research funding associated with this study.

Availability of data and materials
The authors confirm that the data supporting the findings of this study are available within the article and its supplementary materials. Moreover, they are available from the corresponding author (C.Conti) on request.

Declarations

Competing interests
No competing interests associated with this study.

Author details
[1]Institute of Heritage Science (ISPC), National Research Council (CNR), Via Cozzi 53, 20125 Milano, Italy. [2]Cincinnati Art Museum, 953 Eden Park Drive, Cincinnati, USA. [3]Department of Chemistry, University of Cincinnati, 312 College Dr., Cincinnati, USA.

Received: 27 April 2022 Accepted: 24 July 2022
Published online: 09 August 2022

References:

1. Zanesville Art Center Collection, Los Angeles County Museum of Art, Overseas Archaeological Exhibitions Corporation. The quest for eternity: Chinese ceramic sculptures from the People's Republic of China. Los Angeles County Museum of Art; Chronicle Books; 1987.
2. Ramacciotti M, Gallello G, Navarro-Martosa D, Doménech-Carbó A, Roldán C, Hernández E, Garrigues S, Pastor A. An innovative multi-analytical approach based on spectroscopic and electrochemical techniques to study a complex Roman amphorae collection. Appl Clay Sci. 2020;198: 105857.
3. Sciau P, Sanchez C, Gliozzo E. Ceramic technology: how to characterize terra sigillata ware. Archaeol Anthropol Sci. 2020;12:211.
4. Calparsoro E, Sanchez-Garmendia U, Arana G, Maguregui M, Iñañez JG. An archaeometric approach to the majolica pottery from alcazar of Nájera archaeological site. Herit Sci. 2019;7:33.
5. Ma X, Berrie BH. Lead Chlorides in Paint on a Della Robbia Terracotta Sculpture. Anal Chem. 2020;92:4935.
6. Raneri S, Venturi F, Palleschi V, Legnaioli S, Lezzerini M, Pagnotta S, Ramacciotti M, Gallello G. Social and technological changes in the ceramic production of the Northern Levant during the LBA/IA transition: New evidence about the Sea People issue through archaeometry. Anthropol Archaeol. 2019;56:101087.
7. Di Bella M, Mastelloni MA, Baldanza A, Quartieri S, Italiano F, Tripodo A, Romano D, Leonetti F, Sabatino G. Archaeometric constraints by multidisciplinary study of Richborough 527 amphorae and yellow clays from the C.da Portinenti pottery workshop (Lipari Island, Italy). Arch Anthr Sci. 2019;11:2957.
8. Ferri TZ, Rončević S, Lipovac Vrkljan G, Konestra A. Post-depositional alterations of terrestrial and marine finds of Roman ceramics from Crikvenica production centre (NE Adriatic, Croatia) – A contribution towards chemometric classification. J Cult Herit. 2020;43:1.
9. González-Miranda FM, Garzón E, Reca J, Pérez-Villarejo L, Martínez-Martínez S, Sánchez-Soto PJ. Thermal behaviour of sericite clays as precursors of mullite materials. J Therm Anal Calorim. 2018;132:967.
10. Nandi VS, Raupp-Pereira F, Montedo ORK, Oliveira APN. The use of ceramic sludge and recycled glass to obtain engobes for manufacturing ceramic tiles. J Cleaner Prod. 2015;86:461.
11. Mahmoudi S, Srasra E, Zargouni F. Composition and ceramic properties of carbonate-bearing: illitic clays from North-Eastern Tunisia. Arab J Sci Eng. 2014;39:5729.
12. Jusnes KF, Tangstad M, Ringdalen E. Phase Transformations from Quartz to Cristobalite. In: Davis B (eds) The Minerals, Metals & Materials Series. Springer, Cham. 2018
13. Lee WE, Souza GP, McConville CJ, Tarvornpanich T, Iqbal Y. Mullite formation in clays and clay-derived vitreous ceramics. J Eur Ceramic Soc. 2008;28:465–71.
14. Abdullah MAK, Hassan AH, Hala AM, Mona FA. Mineralogical characterization of Islamic stucco: Minaret of Shams El-Deen El-Wasty, Bulaq. Egypt Construct Build Mat. 2015;101:692.
15. Freire MT, Veiga MR, Silva AS, de Brito J. Restoration of ancient gypsum-based plasters: Design of compatible materials. Cem Concr Compos. 2021;120:977.
16. Nunes S, Ramacciotti F, Neves A, Angelin EM, Ramos AM, Roldão É, Wallaszkovits N, Armijo AA, Melo MJ. A diagnostic tool for assessing the conservation condition of cellulose nitrate and acetate in heritage collections: quantifying the degree of substitution by infrared spectroscopy. Herit Sci. 2020;8:33.
17. Quye A, Littlejohn D, Pethrick RA, Stewart RA. Investigation of inherent degradation in cellulose nitrate museum artefacts. Polymer Degrad Stabil. 2011;96:1369.
18. Doménech-Carbó MT, Doménech-Carbó A, Gimeno-Adelantado JV, Bosch-Reig F. Identification of Synthetic Resins Used in Works of Art by Fourier Transform Infrared Spectroscopy. Appl Spectrosc. 2001;55:1590.
19. Vichi A, Eliazyan G, Kazarian SG. Study of the degradation and conservation of historical leather book covers with macro attenuated total reflection-Fourier Transform Infrared Spectroscopic Imaging. ACS Omega. 2018;3:7150.
20. Ricci C, Bloxham S, Kazarian SG. ATR-FTIR imaging of albumen photographic prints. J Cult Herit. 2007;8:387.
21. Neves A, Angelin EM, Roldão É, Melo MJ. New insights into the degradation mechanism of cellulose nitrate in cinematographic films by Raman microscopy. J Raman Spectrosc. 2019;50:202.
22. Bussiere PO, Gardette JL, Theriasac S. Photodegradation of celluloid used in museum artifacts. Polymer Degrad Stabil. 2014;107:246.
23. Ruiz-Agudo E, Putnis CV, Hovelman J, Alvarez-Lloret P, Albanez-Velasco A, Putnis A. Experimental study of the replacement of calcite by calcium sulphates. Geochim Cosmochim Acta. 2015;156:75.
24. Mazurek J, Laganà A, Dion V, Etyemez S, Carta C, Schilling MR. Investigation of cellulose nitrate and cellulose acetate plastics in museum collections using ion chromatography and size exclusion chromatography. J Cult Herit. 2019;35:263.

Publisher's Note